

CrossMark
click for updates

Cite this: DOI: 10.1039/c6ta08652g

Received 6th October 2016
Accepted 5th December 2016

DOI: 10.1039/c6ta08652g

www.rsc.org/MaterialsA

An antimonate pyrochlore ($\text{H}_{1.23}\text{Sr}_{0.45}\text{SbO}_{3.48}$) for photocatalytic oxidation of benzene: effective oxygen usage and excellent activity†

Jing Chen, Yu Shao and Danzhen Li*

The sample $\text{H}_{1.23}\text{Sr}_{0.45}\text{SbO}_{3.48}$ crystallized in a pyrochlore structure is applied to photocatalytic oxidation of benzene in the gaseous phase. The pyrochlore structure is considered as the key factor for the effective oxygen adsorption, which makes the sample exhibit excellent photocatalytic activity.

Benzene is one of the most fundamental organic materials. Many important chemical compounds, such as phenol, toluene, aniline, biphenyl, naphthalene, anthracene and dioxin, are derived from benzene by replacing one or more of its hydrogen atoms with another functional group. However, benzene and most of its derivatives are poisonous. Thus, the cleavage of the aromatic ring into low-toxic or non-toxic molecules is an important issue. Photocatalytic oxidation (PCO) using TiO_2 has attracted considerable interest as a promising technology for deep oxidation of benzene at room temperature.¹ However, the low quantum yield of TiO_2 due to fast recombination of photo-generated electrons and holes greatly hampers its extensive application for the removal of benzene. Several approaches have been explored for the improvement of the PCO quantum yield, such as developing new photocatalysts as alternatives to TiO_2 and the combination of H_2O , H_2 or thermal energy into photocatalysis for obtaining the synergy effect.² Great progress has been made in this field, such as $\text{ZnSn}(\text{OH})_6$, $\beta\text{-Ga}_2\text{O}_3$ and vanadate/ TiO_2 composites (Table S1†). Such studies pointed out that both of hydroxyl radical ($\cdot\text{OH}$) and super oxide radical ($\text{O}_2^{\cdot-}$) are the main active species during the benzene oxidation. However, the mechanism of this reaction is very similar even over different photocatalysts. The issue of how to choose an efficient photocatalyst for degradation of benzene is seldom discussed in these studies. The key influencing factor during

the oxidation of benzene is also ambiguous, which hampers the development of an appropriate photocatalyst.

To develop an efficient photocatalyst for degradation of benzene, efficient carrier capture is indispensable. Generally, the photogenerated electrons and holes are captured by the surface-adsorbed O_2 and surface-adsorbed hydroxyl groups, respectively. The oxidation reactions are reported to occur by either indirect oxidation *via* the surface-bound hydroxyl radicals and directly *via* the valence-band holes.³ However, in the consideration of the kinetic factor, the capture of photo-generated electrons by the surface-adsorbed O_2 is relatively slow (about 10 μs) and acts as a rate determining reaction.⁴ This is very important but often neglected in the previous studies listed in Table S1.† Thus, it is greatly desired to develop new photocatalysts to promote the adsorption of O_2 for increasing the quantum efficiency of PCO.

In this paper, we are intrigued by the pyrochlore compound. The pyrochlore structure has Fd-3m symmetry. The general composition of a typical pyrochlore oxide is $\text{A}_2\text{B}_2\text{O}_6\text{O}'$ ($\text{A}_2\text{B}_2\text{O}_7$). The crystallographic structure consists of the B_2O_6 open framework built by corner-sharing BO_6 octahedra and the $\text{A}_2\text{O}'$ chains filled in the interstitial sites. The interactions between the B_2O_6 framework and $\text{A}_2\text{O}'$ chains are weak, leading to the absence of A or O' and the formation of defect pyrochlore.⁵ In terms of electronic structure, a previous calculation has pointed out that the 5s and 5p orbitals of the M cation ($\text{M} = \text{Sn}$ or Sb) form covalent interactions with the O 2p orbitals. The LUMO consists of Sb 5s-O 2p interaction, while the HOMO is made up of nonbonding O 2p states, when the A cation is Ca, Sr and Ba).⁶ The band gap of this kind of antimonate mainly depends on the cation at the B site, and the orbitals of A and O' contribute nothing to the HOMO and LUMO, but the defect in the $\text{A}_2\text{O}'$ chains will drive the migration of O in the B_2O_6 framework.⁷ The unique crystalline and electronic structure makes pyrochlore sustain a range of functions including as an oxygen electrocatalyst, in lithium- O_2 batteries, and as an oxygen storage material.⁸ Besides, pyrochlore can act as a proton conductor by allowing protons to diffuse along the O in the B_2O_6 framework.⁹

State Key Laboratory of Photocatalysis on Energy and Environment, Research Institute of Photocatalysis, Fuzhou University, Fuzhou, 350002, PR China. E-mail: dzli@fzu.edu.cn; Fax: +86-591- 83779256; Tel: +86-591- 83779256

† Electronic supplementary information (ESI) available. See DOI: 10.1039/c6ta08652g

This proton conduction mechanism in the pyrochlore-structured compound leads to the highly hydroxylated surface of pyrochlore, which is beneficial for increasing the adsorption of oxygen on the surface.¹ Thus, the pyrochlore is a favourable candidate for improving the oxidation reactions. To our knowledge, photocatalysts with the pyrochlore structure have been applied to the degradation of benzene. However, the superiority of this structure has not been revealed.¹⁰

A series of strontium antimonate photocatalysts (denoted as SSO-pH) are prepared using potassium pyroantimonate and strontium chloride as precursors at pH = 4–9 by a simple hydrothermal method (see the Experimental Section in the ESI†). The transmission electron microscopy (TEM) of the SSO-8 shows that the sample consists of mainly 11–13 nm particles (Fig. 1(a)). The clear lattice fringe (0.581 nm) corresponding to the (111) planes throughout each nanoparticle and the clear spot array of the FFT pattern suggest the single crystalline nature of these nanoparticles. We then determine the Sr/Sb ratio of SSO-8 using an X-ray photoelectron spectroscope (XPS) and an energy dispersive spectrometer (EDS) equipped on a scanning electron microscope. The Sr/Sb ratio obtained from EDS and XPS is 0.43/1 and 0.48/1, respectively. The X-ray diffraction (XRD) pattern of the SSO-8 (Fig. 1(b)) indicates that it crystallizes in the pyrochlore structure (ICSD-72097).¹¹ The structure adopts space group $Fd\bar{3}m$ (227) and has a cubic lattice

parameter of $a = 10.37 \text{ \AA}$. In this structure, Sb (mixed valence and B site cation, Fig. S1 and Table S2†) and O_{48f} atoms, consisting of the SbO_6 octahedron, are placed on the 16c site (0, 0, 0) and the 48f site (0.3186, 1/8, 1/8), respectively. The corner-sharing SbO_6 octahedron creates a three-dimensional open framework (the inset of Fig. 1(b)). The Sr^{2+} cation (A site cation) occupies the highly symmetrical position (32e, $\bar{3}m$) which is in the cage formed by the SbO_6 octahedron (Fig. S2†). The formula of SSO-8 is $H_{1.23}Sr_{0.45}SbO_{3.48}$ ($R_{wp} = 3.50\%$, $R_p = 2.93\%$, $\chi^2 = 1.895$, Table S1†), and H^+ is added to maintain electrical neutrality. The XRD patterns of other samples are shown in Fig. S3a.† The variation of peak strength corresponding to the (111) plane illustrates the different occupancy of the A site.¹² The content of the oxygen adsorbed on the surface of SSO-8 is also displayed in Fig. S1.† The binding energy of 530.04, 531.31 and 532.41 eV corresponds to the lattice oxygen, adsorbed oxygen and surface hydroxyl, respectively.¹³ Thus, the adsorbed oxygen on the surface of SSO-8 is abundant.

Photocatalytic oxidation of 312 ppm gaseous benzene at a certain gas hourly space velocity (GHSV) is used as the probe reaction. The photocatalytic activity of samples synthesized at different pH values is shown in Fig. S4,† and the photocatalytic activity of the samples is related to their specific surface area (Fig. S3b†) and SSO-8 is the best sample. Fig. 2 shows that the conversion and mineralization ratios (C_R and M_R) of the photocatalytic oxidation of benzene over SSO-8 are up to 100% and 74% ($GHSV \sim 3000 \text{ h}^{-1}$), which are about 10 and 5 times higher than those of P25. The quantum yield (QY) on the SSO-8 and P25 is calculated to be ca. 29.7% and 1.32%, respectively (Table S3 and 4†, the radiant illuminance of the light source is shown in Fig. S5†). To evaluate the stability, photocatalytic oxidation of benzene is measured at different GHSVs ($4285.7\text{--}11538.5 \text{ h}^{-1}$) for 42 h (Fig. S6†). When the GHSV is increased to 11538.5 h^{-1} , the C_R and M_R of benzene still remained at 37.7% and 74% after 42 hours indicating a good stability of photocatalytic activity of SSO-8. In addition, the same XRD and XPS patterns before and after the reaction suggest the stable structure of SSO-8 (Fig. S7†). From Table S1,† $ZnSn(OH)_6$ and $\beta\text{-Ga}_2\text{O}_3$ are considered as excellent photocatalysts. To evaluate the photocatalytic activity of the SSO-8 further, we select the $ZnSn(OH)_6$ and $\beta\text{-Ga}_2\text{O}_3$ as the

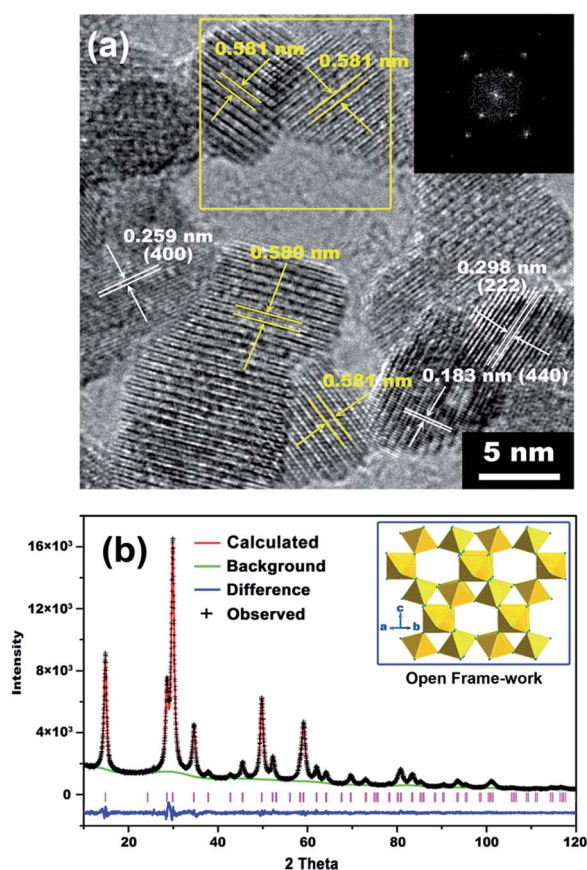


Fig. 1 (a) TEM image of SSO-8 (inset: the FFT pattern). (b) XRD pattern of SSO-8 (inset: the open framework of the corner-sharing SbO_6).

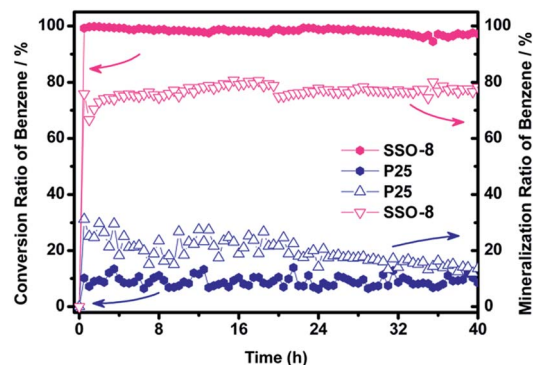


Fig. 2 The C_R and M_R of C_6H_6 over SSO-8 and P25 ($GHSV \sim 3000 \text{ h}^{-1}$).

reference. As shown in Fig. S8,† the SSO-8 still exhibits the best photocatalytic activity.

The influence of the O_2 concentration in atmosphere on SSO-8 is investigated (Fig. 3(a) and S9(a) and (b)†). The C_R of benzene over SSO-8 drops with the decreased O_2 concentration. The variation of M_R is different from the C_R . Under anaerobic conditions ($O_2 : N_2 = 0 : 100$), the M_R of benzene is only 15%, while it grows up to 74% when the O_2 concentration increases to only 3%. A similar control experiment is conducted over the P25 (Fig. 3(a) and S9(c) and (d)†), and both the C_R and M_R of benzene decrease with the drop of the O_2 concentration. P25 does not show photocatalytic activity when the O_2 concentration is 3%. These results indicate that (1) the photocatalytic activity is affected greatly by the concentration of O_2 , and (2) the utilization efficiency of O_2 over SSO-8 is better than that over P25. To investigate the role of O_2 further, H_2O is introduced into the system as the origin of oxygen instead of O_2 (Fig. S10†). In this case, holes can be captured on the hydroxyl groups to form hydroxyl radicals ($\cdot OH$), and the consumed hydroxyl groups will be compensated by the decomposition of H_2O into two hydroxyl groups at the oxygen vacancy on the surface of the photocatalyst. Under anaerobic conditions, P25 does not show photocatalytic activity whether the water vapor is introduced into the system or not. In the case of SSO-8, 10% benzene has been decomposed in the dry N_2 flow, and the addition of water vapor decreases the C_R slightly. Although the M_R soars to 100% as soon as the water vapor is introduced into the system, it decreases sharply as time goes by. Therefore, $-OH/\cdot OH$ and holes play a limited role during the oxidation of benzene without O_2 .

The reactive oxygen species (ROS) such as hydroxyl radicals ($\cdot OH$) and superoxide radicals ($O_2^{\cdot -}$) are the products of carrier capture, which are indispensable for further photochemical reactions. The UV-Vis absorption spectrum of SSO-8 reveals that

the indirect band gap of SSO-8 is 4.1 eV. The Mott–Schottky (M–S) plots show that the conduction band (CB) position is at -0.3 V vs. standard hydrogen electrode (SHE). Therefore, the CB and VB positions of SSO-8 are suitable for the production of $\cdot OH$ ($\cdot OH/H_2O$ 2.27 V vs. SHE, pH = 7) and $O_2^{\cdot -}$ ($O_2/O_2^{\cdot -}$ -0.28 V vs. SHE, pH = 7) (Fig. S11†). The relative content of $\cdot OH$ and $O_2^{\cdot -}$ is determined by the ESR spin trapping technique. When 5,5-dimethyl-1-pyrroline *N*-oxide (DMPO) is used as a spin trapping agent, the $DMPO/O_2^{\cdot -}$ transfers to $DMPO/\cdot OH$ in water quickly.¹⁴ Therefore, 5-tertbutoxycarbonyl-5-methyl-1-pyrroline *N*-oxide (BMPO) is selected as a spin trapping agent, because both of the $BMPO/O_2^{\cdot -}$ and $DMPO/\cdot OH$ are stable in water.¹⁵ In this case, the origin of $O_2^{\cdot -}$ and $\cdot OH$ is considered to be e^-/O_2 and $h^+/-OH$, respectively. Fig. 3 (b) and (c) illustrate the ESR spectra of $O_2^{\cdot -}$ and $\cdot OH$ formed during photoexcitation of SSO-8 and P25. No ESR signal is observed for samples without irradiation or photocatalysts. Upon irradiation, a four-line spectrum with relative intensities of 1 : 2 : 2 : 1 can be observed, which is the adduct formed between BMPO and the hydroxyl radical ($BMPO/\cdot OH$) or superoxide ($BMPO/O_2^{\cdot -}$). Since the $BMPO/\cdot OH$ and $BMPO/O_2^{\cdot -}$ have overlapping ESR spectra, whether the ESR signal in part comes from the $O_2^{\cdot -}$ should be determined. Dimethyl sulfoxide (DMSO, 12%) and superoxide dismutase (SOD, 600 U ml⁻¹) are used to quench the $\cdot OH$ and $O_2^{\cdot -}$, respectively.^{15,16} The scavenging effects of DMSO and SOD on the ESR signals from both photocatalysts are investigated. When the photocatalysts are irradiated by UV light, we found that the total amount of $\cdot OH$ and $O_2^{\cdot -}$ from SSO-8 is larger than that from P25. The addition of SOD leads to significant reduction of $O_2^{\cdot -}$ and the residual signal can be assigned to the $BMPO/\cdot OH$ adduct, which indicates that (1) SSO-8 produces more $O_2^{\cdot -}$ and $\cdot OH$ than P25, and (2) O_2 not only improves the separation of e^- and h^+ , but also acts as the main source of ROS. The addition of DMSO for scavenging of $\cdot OH$ illustrates the same results.

To investigate the adsorption of oxygen further, we analysed the ROS by O_2 temperature programmed desorption (O_2 -TPD). The oxygen adsorption proceeds by the following procedure: O_2 (ad) $\rightarrow O_2^{\cdot -}$ (ad) $\rightarrow O^-$ (ad) $\rightarrow O^{2-}$ (lattice).¹⁷ As shown in Fig. 4(a), the O_2 -TPD profiles of SSO-8 and P25 show three desorption peaks corresponding to desorption of $O_2^{\cdot -}$ (≤ 180 °C), O^- (≤ 500 °C) and lattice oxygen at higher temperatures, respectively. The peak at 300 °C in the profile of SSO-8 and the peak at 450 °C in the profile of P25 are recognized as the O^- (ad). Since the electrophilic reaction between O^- or $O_2^{\cdot -}$ and benzene is beneficial for the total oxidation of benzene, the large desorption amount and the lower desorption temperature of O^- (ad) on the SSO-8 mean the higher oxidation ability of SSO-8. In addition, the irradiation during the pretreatment process increases the desorption amount of O^- (ad) indicating that the production of O^- (ad) can be a photochemical process.

Water desorption profiles during the O_2 -TPD process are recorded simultaneously with the oxygen desorption profiles (Fig. 4(b)). The water peak area of SSO-8 is larger than that of P25 indicating much more water desorption from SSO-8 during the O_2 -TPD process. Notably, the highest water peak is at the same temperature (300 °C) as the O^- (ad) peak, and the decrease

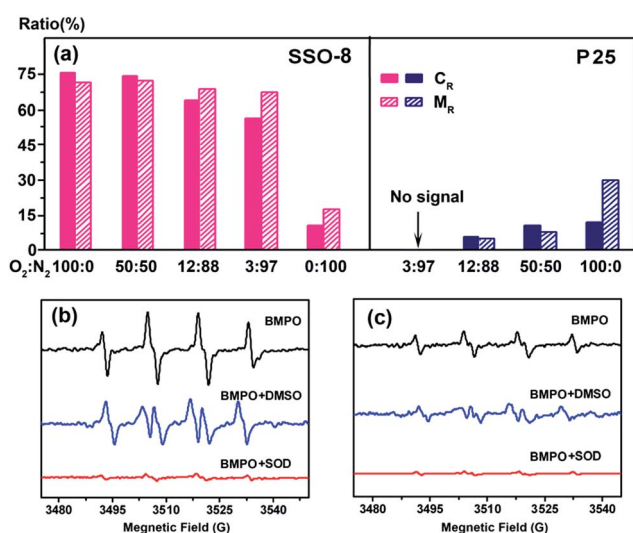


Fig. 3 (a) The C_R and M_R of benzene in different atmospheres over SSO-8 and P25 (GHSV ~ 4000 h⁻¹). (b) The ESR signals generated from SSO-8. (c) The ESR signals generated from P25. All of the samples are irradiated by UV light (centered at 254 nm).

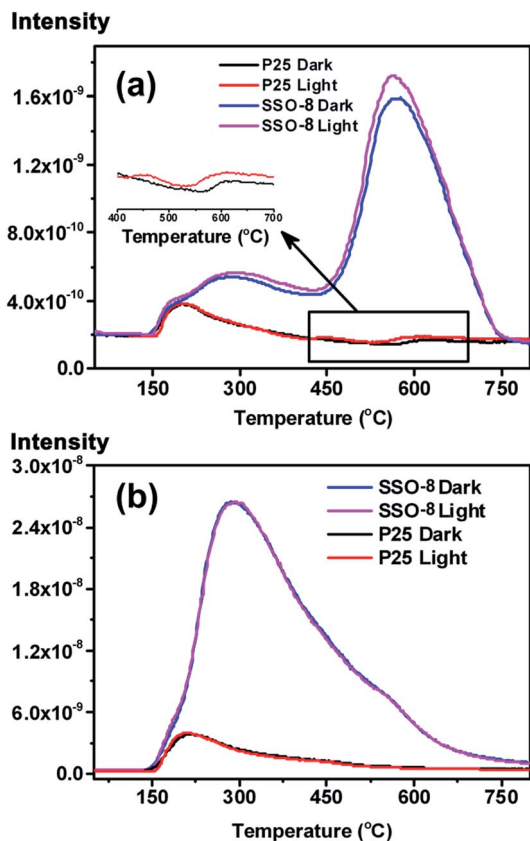
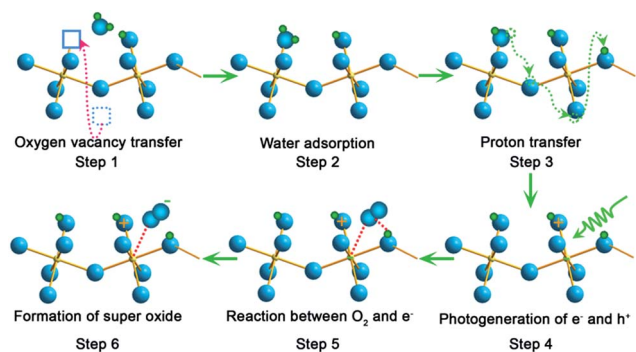


Fig. 4 (a) The O_2 -TPD profiles of SSO-8 and P25. (b) The desorption of H_2O from SSO and P25 during the O_2 -TPD process.

of the pretreatment temperature from 180 °C to 80 °C leaves more oxygen species and hydroxyl groups on the surface (Fig. S12[†]). These results suggest the proportional relationship between surface hydroxyl groups and adsorbed oxygen. Thus, the PCO activity will be increased in the water vapor, which is confirmed by Fig. S13.[†]

From the above discussion, it is clear that the large amount of surface-adsorbed O_2 is a key factor for good photocatalytic activity. A detailed description about why SSO-8 is suitable for the absorption of O_2 is as follows. As shown in Scheme 1, SSO-8 adopts a pyrochlore structure which is non-stoichiometric according to its formula. The intrinsic oxygen vacancy in the 8b



Scheme 1 Adsorption of O_2 on the surface of SSO-8.

site allows the oxygen ion in the 48f site to move to the 8b site, leaving an oxygen vacancy in the 48f site (step 1).⁷ When a water molecule is absorbed on the 48f oxygen vacancy of SSO, it decomposes into two surface hydroxyl groups quickly (step 2). Step 3 often takes place on a proton conductor. To verify the proton conductivity of SSO-8, impedance spectra of SSO and P25 are recorded in a H_2 atmosphere and vacuum (Fig. S14[†]). The conductivity of P25 shows no difference between the H_2 atmosphere and vacuum, while the conductivity of SSO-8 in the H_2 atmosphere is higher than that in vacuum. This confirms that the protons can diffuse into the bulk of SSO-8, and the proton-conducting properties contribute to forming more OH groups by transferring protons *via* single OH bond formation in the crystal (particularly with O^{2-} ions on 48f sites).⁹ Thus, SSO-8 has a highly hydroxylated surface, which is suitable for O_2 adsorption. In steps 4, 5 and 6, the oxygen adsorbs on the surface hydroxyl group and forms superoxide. Then, the O^- or $\cdot OH$ with stronger oxidation ability will be formed *via* a series of reactions with superoxide (Scheme 1).

In summary, we have prepared a series of antimonate pyrochlores by a simple hydrothermal method. Photocatalytic oxidation of benzene is chosen as the probe reaction. When the GHSV is 3000 h^{-1} , the conversion and mineralization ratios of photocatalytic benzene oxidation over $H_{1.23}Sr_{0.45}SbO_{3.48}$ are up to 100% and 74%, which are about 10 and 3 times higher than those of P25. Then, we demonstrated that the photooxidation of benzene over the antimonate pyrochlore depends on the efficiency of oxygen usage greatly, and the highly hydroxylated surface caused by the proton conductivity of the pyrochlore plays a key role for the improvement of the adsorption of oxygen. We envision that this discovery will lead to further development of highly efficient photocatalysts for photooxidation of benzene.

Acknowledgements

This work was financially supported by the NNSF of China (21173047 and 21373049).

References

- 1 X. Fu, J. Wang, D. Huang, S. Meng, Z. Zhang, L. Li, T. Miao and S. Chen, *ACS Catal.*, 2016, **6**, 957–968.
- 2 Y. Luo, J. Chen, J. Liu, Y. Shao, X. Li and D. Li, *Appl. Catal., B*, 2016, **182**, 533–540; J. Wang, H. Ruan, W. Li, D. Li, Y. Hu, J. Chen, Y. Shao and Y. Zheng, *J. Phys. Chem. C*, 2012, **116**, 13935–13943; X. Z. Fu, W. A. Zeltner and M. A. Anderson, *Appl. Catal., B*, 1995, **6**, 209–224; Y. L. Chen, D. Z. Li, X. C. Wang, X. X. Wang and X. Z. Fu, *Chem. Commun.*, 2004, **20**, 2304–2305.
- 3 M. R. Hoffmann, S. T. Martin, W. Choi and D. W. Bahnemann, *Chem. Rev.*, 1995, **95**, 69–96.
- 4 Z. Li, Y. Luan, Y. Qu and L. Jing, *ACS Appl. Mater. Interfaces*, 2015, **7**, 22727–22740.
- 5 R. R. Jitta, R. Gundeboina, N. K. Veldurthi, R. Guje and V. Muga, *J. Chem. Technol. Biotechnol.*, 2015, **90**, 1937–1948.

- 6 H. Mizoguchi, H. W. Eng and P. M. Woodward, *Inorg. Chem.*, 2004, **43**, 1667–1680.
- 7 D. S. D. Gunn, N. L. Allan, H. Foxhall, J. H. Harding, J. A. Purton, W. Smith, M. J. Stein, I. T. Todorov and K. P. Travis, *J. Mater. Chem.*, 2012, **22**, 4675.
- 8 T. Iwanaga, S. Takase and Y. Shimizu, *ECS Trans.*, 2008, **16**, 955–959; S. H. Oh, R. Black, E. Pomerantseva, J. H. Lee and L. F. Nazar, *Nat. Chem.*, 2012, **4**, 1004–1010; B. Tolla, A. Demourgues, O. Isnard, M. Menetrier, M. Pouchard, L. Rabardel and T. Seguelong, *J. Mater. Chem.*, 1999, **9**, 3131–3136.
- 9 K. Toyoura, A. Nakamura and K. Matsunaga, *J. Phys. Chem. C*, 2015, **119**, 8480–8487.
- 10 M.-C. Hsieh, G.-C. Wu, W.-G. Liu, W. A. Goddard III and C.-M. Yang, *Angew. Chem., Int. Ed.*, 2014, **53**, 14216–14220; B. Kiss, C. Didier, T. Johnson, T. D. Manning, M. S. Dyer, A. J. Cowan, J. B. Claridge, J. R. Darwent and M. J. Rosseinsky, *Angew. Chem., Int. Ed.*, 2014, **53**, 14480–14484; S. Uma, J. Singh and V. Thakral, *Inorg. Chem.*, 2009, **48**, 11624–11630; M. Sun, D. Z. Li, Y. Zheng, W. J. Zhang, Y. Shao, Y. B. Chen, W. J. Li and X. Z. Fu, *Environ. Sci. Technol.*, 2009, **43**, 7877–7882; R. Huang, X. Xu, J. Zhu, W. Liu, R. Yuan, X. Fu, Y. Zhang and Z. Li, *Appl. Catal., B*, 2012, **127**, 205–211.
- 11 M. A. Subramanian, G. Aravamudan and G. V. Subba Rao, *Prog. Solid State Chem.*, 1983, **15**, 55–143.
- 12 J. Shi, L. Ma, P. Wu, Z. Zhou, P. Guo, S. Shen, D. Jing and L. Guo, *Nano Res.*, 2012, **5**, 576–583.
- 13 G. Lu, S. L. Bernasek and J. Schwartz, *Surf. Sci.*, 2000, **458**, 80–90.
- 14 E. Finkelstein, G. M. Rosen and E. J. Rauckman, *J. Am. Chem. Soc.*, 1980, **102**, 4994–4999; E. Finkelstein, G. M. Rosen, E. J. Rauckman and J. Paxton, *Mol. Pharmacol.*, 1979, **16**, 676–685.
- 15 W. He, H. K. Kim, W. G. Wamer, D. Melka, J. H. Callahan and J. J. Yin, *J. Am. Chem. Soc.*, 2014, **136**, 750–757.
- 16 W. Xu, P. K. Jain, B. J. Beberwyck and A. P. Alivisatos, *J. Am. Chem. Soc.*, 2012, **134**, 3946–3949.
- 17 G. Zou, Y. Xu, S. Wang, M. Chen and W. Shangguan, *Catal. Sci. Technol.*, 2015, **5**, 1084–1092; A. Gurlo, *ChemPhysChem*, 2006, **7**, 2041–2052.